Scripta Materialia 190 (2021) 121–125

Contents lists available at ScienceDirect

Scripta Materialia

journal homepage: www.elsevier.com/locate/scriptamat

Dislocation networks in gamma/gamma'-microstructures formed during selective laser melting of a Ni-base superalloy

L. Heep[a,*], C. Schwalbe[b], C. Heinze[c], A. Dlouhy[d], C.M.F. Rae[b], G. Eggeler[a]

[a] Institute for Materials, Ruhr-University Bochum, 44801 Bochum, Germany
[b] Department of Materials Science and Metallurgy, University of Cambridge, Cambridge CB2 3QZ, UK
[c] Corporate Technology, Siemens AG, 13629 Berlin, Germany
[d] Institute of Physics of Materials, Academy of Sciences of the Czech Republic, 616 62 Brno, Czech Republic

ARTICLE INFO

Article history:
Received 7 July 2020
Revised 20 August 2020
Accepted 20 August 2020
Available online 4 September 2020

Keywords:
Dislocation networks
Ni-base superalloys
Merging γ'-particles
Scanning transmission electron microscopy
Anti-phase boundary energies

ABSTRACT

A dislocation network which formed during selective laser melting (SLM) of a Ni-base superalloy was analyzed using scanning transmission electron microscopy (STEM). This network traverses an ordered Gamma'-phase domain, in between two adjacent Gamma-solid solution regions. The Gamma'-phase region has formed when two Gamma'-phase particles have started to coalesce, trapping the dislocation network in this ordered region so that it formed two dislocation families with pairs of anti-phase boundary (APB) coupled super partial dislocations. The network features are presented and unusual features (twist character and low APB energies), not previously reported, are discussed.

The excellent high temperature strength of Ni-base superalloys relies on a microstructure where $L1_2$ ordered γ'-phase particles precipitate coherently in a cubic face centered γ-matrix [1]. The γ'-particles nucleate and grow during processing. Their volume fraction, size, shape and chemical composition depends on alloy composition and on the processing parameters [2]. CM247LC is an alloy with a negative misfit, where the lattice constant of the γ'-particles is smaller than the lattice constant of the γ-phase. This lattice misfit gives rise to high local stresses, where high compressive stresses in the channels are balanced by tensile stress components in the γ'-particles [3,4]. During high temperature exposure, the misfit can be relieved by the formation of networks of edge dislocations at the interfaces between the two phases [4,5].

In the present work we investigate a dislocation network which has formed in a heat-treated polycrystalline superalloy of type CM247LC which was produced by selective laser melting (SLM). For the scientific objectives of the present work details of alloy composition, processing and heat treatment are not the principal focus. It is however relevant that SLM processing can introduce subgrains into the microstructure and the low angle grain boundaries between them appear as dislocation networks running through the γ/γ' microstructure. High local stresses can also drive microstructural evolution including directional coarsening and coalescence of the γ' [6–8], and thus the evolution of the misfit networks between the γ and γ' phases [4,5,9–11].

Under appropriate thermomechanical conditions γ' coalesce in single crystal superalloys produces rafting and topological inversion [12,13]. In the present work we investigate a dislocation network accommodating misorientation rather than misfit. The network stretches from one γ-region to another over a γ'-neck, which connects to γ'-regions which have just started to coalesce. We investigate how the trapped dislocation network reacts to the imposed γ'-order and how the microstructural data can be used to determine anti phase boundary (APB) energies in the γ'-phase.

In the present study, we investigated the polycrystalline superalloy CM247LC which was developed for directional solidification (DS) processing [14]. Its chemical composition is given in Table 1. It contains Hf for grain boundary strength and relies on γ'-precipitation hardening for resistance to high temperature plasticity [15].

The material investigated was produced by selective laser melting (SLM) in the shape of 30 × 30 × 5 mm^3 plates. Its heat treatment after SLM processing consisted of solution annealing at 1232 °C (2 h), and a two-step precipitation treatment at 1080 °C (2 h) and 870°C (20 h). It is well known that SLM can be used to fabricate geometrically complex parts directly from CAD data. But it is also well known that during SLM processing, the laser beam generates rapid heating and cooling cycles associated with thermal gradients and internal stresses which may even lead to cracking

* Corresponding author.
E-mail address: larissa.heep@rub.de (L. Heep).

https://doi.org/10.1016/j.scriptamat.2020.08.019

Table 1
Average chemical composition of CM247LC in wt.-percentage.

Al	B	C	Co	Cr	Hf	Mo	Ta	Ti	W	Zr	Ni
5.6	0.015	0.07	9.0	8.0	1.4	0.5	3.2	0.7	10.0	0.01	Bal.

[15,16]. So, whilst SLM has many features in common with DS processing of superalloys, there are also important differences.

Both, conventional DS processing and SLM processing create polycrystalline microstructures. Conventional DS processing creates polycrystals, where longitudinal grains (dendrites) have common [001] orientations. As the common rotation axis lies in the (vertical) boundary plane, these boundaries all have 'tilt' character. Attempts have been made to interpret the misorientations between DS dendrites on the basis of regular subgrain boundaries [17]. The SLM microstructures investigated in the present work do not exhibit the common [001] direction associated with DS processing (not shown here). Instead they represent polycrystalline systems with both high and low angle grain boundaries. In the present work we focus on a specific low angle grain boundaries in a SLM microstructure. We show a SLM subgrain boundary which has not previously been described for alloys which were produced in a DS process. This particular boundary represents a rotation around an axis perpendicular to the boundary plane and is hence a 'twist' boundary.

The dislocation substructure investigated in the present work was characterized using diffraction contrast scanning transmission electron microscopy (STEM). Thin foils were obtained by electrochemical thinning of 3 mm/200 µm in a Struers twin jet Tenupol-5 electropolisher, using an electrolyte consisting of 6 vol.-% perchloric acid in methanol at -5 (±1) °C and a voltage of 13 V. STEM investigations were performed using a JEOL JEM-2100 microscope operating at 200 kV. Our TEM methodology has been described in detail in previous publications [e.g. 18,19] and we use our cube projection method [20] for documenting orientations and our anaglyph stereo method [21] for investigating the spatial arrangement of microstructural elements.

Fig. 1 shows a micrograph and three schematic illustrations describing the local microstructure and our TEM procedure. Fig. 1a is a multiple beam STEM image taken close to the [110]-zone (see Kikuchi pattern inset). The foil direction is given by the cube projection inset in the upper left of the image. A dislocation network traverses the image from the top to the bottom. In the area highlighted with a white rectangle, two network dislocation segment families 1 and 2 form regular pairs, one is parallel to [101] the other to [$\bar{1}$01]. The network regions above and below contain regular segments, which are not paired. Fig. 1b demonstrates that the highlighted region is part of a neck connecting two coalescing γ'-regions. The schematic Kikuchi map in Fig. 1c shows all the tilt positions where two beam diffraction STEM images were taken. Eight contrast conditions were established in the present work (two stereo pairs were taken using $\mathbf{g}_1$=$\mathbf{g}_2$=($\bar{1}$ 1 1) (not shown) and with $\mathbf{g}_4$=$\mathbf{g}_5$=($\bar{1}$ 1 $\bar{1}$). Fig. 1d shows a reference line which intersects regularly spaced dislocation pairs of dislocation family 1 (one pair represented by an upper blue and a lower red circle). These dislocations are oriented end-on in Fig. 1d and we will address their configuration later in calculations of APB energies.

The anaglyph in Fig. 2 was obtained from the stereo pair of STEM images taken at $\mathbf{g}_4$ and $\mathbf{g}_5$ ($\mathbf{g}_4$=$\mathbf{g}_5$=($\bar{1}$ 1 $\bar{1}$)) as described in [21]. When viewed with coloured glasses as indicated (red glass in front of left eye) it aids perception of the spatial arrangement of the dislocation network. The anaglyph in Fig. 2 also integrates a projection of the reference cube [20] which allows direct assessment of the directions of dislocation segments and the spatial orientation of the network plane. For $\mathbf{g}_4$=$\mathbf{g}_5$=($\bar{1}$ 1 $\bar{1}$), dislocation family 1 with segments parallel to [101] is in full contrast. Dislocation family 2 shows only residual contrast (effective invisibility), but Fig. 2 shows that its line segments are parallel to [10$\bar{1}$]. In line with these findings, the network plane is parallel to (0 1 0).

Table 2
All contrast conditions shown in Fig. 1c together with experimentally observed visibilities/invisibilities. **b**-vectors for dislocation families 1 and 2.

Contrast condition (**g**-vector)	Visibility family 1	Visibility family 2
$\mathbf{g}_1$ = ($\bar{1}$ 1 1)	-	+
$\mathbf{g}_2$ = ($\bar{1}$ 1 1)	-	+
$\mathbf{g}_3$ = (0 0 $\bar{2}$)	+	+
$\mathbf{g}_4$ = ($\bar{1}$ 1 $\bar{1}$)	+	-
$\mathbf{g}_5$ = ($\bar{1}$ 1 $\bar{1}$)	+	-
$\mathbf{g}_6$ = (2 $\bar{2}$ 0)	+	+
$\mathbf{g}_7$ = (1 $\bar{3}$ 1)	+	-
$\mathbf{g}_8$ = (1 $\bar{3}$ $\bar{1}$)	-	+
$\mathbf{g}_9$ = ($\bar{3}$ 1 1)	+	+
$\mathbf{g}_{10}$ = (3 $\bar{1}$ 1)	+	+
Resulting $(2/a)\cdot$ **b**	± [101]	± [$\bar{1}$01]

In Fig. 3 we present four examples for STEM micrographs which were taken under different two beam conditions. In Fig. 3a ($\mathbf{g}_1$=($\bar{1}$ 1 1)) dislocation family 1 is invisible while dislocation family 2 is in full contrast. Under the contrast condition of Fig. 3b ($\mathbf{g}_4$ = ($\bar{1}$ 1 $\bar{1}$), dislocation families 1 / 2 are in full/residual contrast. In Fig. 3c and d ($\mathbf{g}_6$ = (2 $\bar{2}$ 0)and $\mathbf{g}_{10}$ = (3 $\bar{1}$ 1)), both families can be clearly seen. Table 2 summarizes all experimentally observed visibilities/invisibilities. As a result, we obtain the Burgers vectors **b** of dislocation families 1 and 2 as b_1= ± $(a_0/2)\cdot$ [101] and b_2=±$(a_0/2)\cdot$ [$\bar{1}$01]. A comparison with the directions given by the cube projection (see yellow and blue lines in Fig. 3a and b) shows that both families have nearly screw character.

Regular arrays of screw dislocations can represent twist boundaries [23]. {001} type twist boundaries have been investigated in pure metals [24–26], and were considered as a special case [27]. The two sets of screw dislocations crossing at right angles and lying on the 001 plane, as identified here, represent a rotation around the plane normal of θ, where sinθ = b/d where b is the Burgers vector and d the dislocation spacing. Using the values of b = 0.506 nm (for a pair of ½<110> dislocations) and d = 56.3 nm, one obtains a rotation angle of 0.52° for this network about the [001] axis. Evaluating Kikuchi patterns taken from the two regions which are separated by the boundary, would allow confirmation of these misorientations in CBED experiments, and further work would be required to perform such measurements on a statistically relevant number of these special small angle boundaries.

In Ni-base super alloys with γ/γ'-microstructures misfit dislocations are a common microstructural feature which are observed after long term temperature exposure and creep [28,29]. However, twist boundaries cause rotations and do not accommodate misfit. We can therefore conclude that the specific boundary we describe in this work is neither a misfit dislocation network nor is it associated with misorientations between dendrites which would produce 'tilt' boundaries.

We now calculate APB energies from the spacings between the coupled super partials of dislocation family 1. In a first order approximation we assume isotropic linear elasticity where the cross interactions between the two dislocation families can be neglected [30]. In Fig 1d, the straight screw dislocations of family 1 are oriented end-on, parallel to the z-axis (orthogonal system: x - [010],

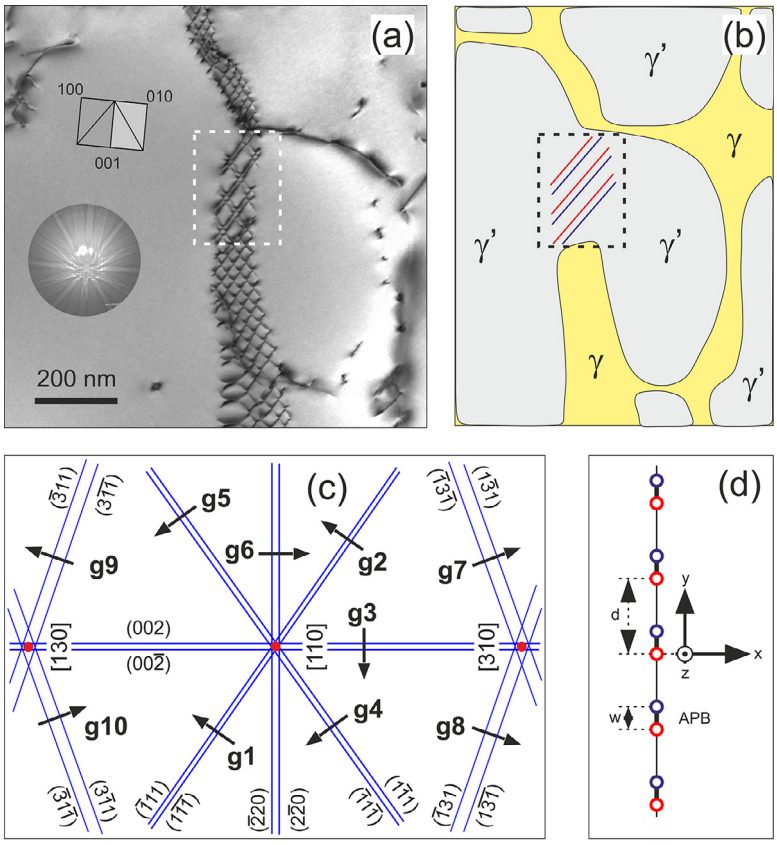

Fig. 1. Dislocation network (experimental image and schematic drawings). (a) Multiple beam contrast STEM micrograph taken close to [110]. (b) Schematic drawing showing that network dislocation pairs are confined to a neck region where two γ'-particles coalesce. (c) Schematic Kikuchi map specifying contrast conditions (diffraction vectors $\mathbf{g_1}$ to $\mathbf{g_{10}}$). (d) Reference line intersecting dislocation pairs (illustrating procedure for APB calculations).

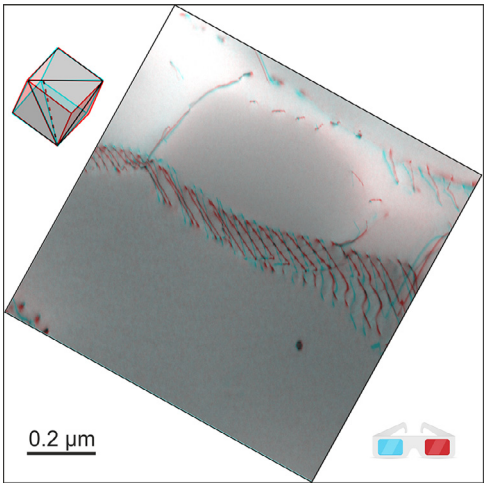

Fig. 2. Spatial impression of the dislocation network. Anaglyph obtained from a stereo pair taken with g-vectors $\mathbf{g}_4$ and $\mathbf{g}_5$ as described in [22]. Viewing the image with coloured glasses (red glass in front of left eye, lower right of image) provides 3D impression. Cube projection in the upper left of image allows to directly appreciate the spatial orientation of lines and planes. (For interpretation of the references to color in this figure legend, the reader is referred to the web version of this article.).

y – [$\bar{1}$ 01]and z - [10 1]). In equilibrium, the repulsive Peach-Köhler force $b \cdot [0, \tau_{xz}, 0]$ acting on each segment of one pair must be balanced by the attractive force associated with the APB energy γ_{APB}. In our estimate we only consider τ_{xz} and neglect all other components of the stress tensor. We use a lattice constant of a_{L12}=0.356 nm [31]. Equilibrium (for the red dislocation segment in the origin of Fig. 1d) requires that $\gamma_{APB} = -b \cdot \tau_{xz}$. The stress component τ_{xz} was calculated for infinite dislocation array ($\tau_{xz}^{fin}(d,w)$) and for a finite number of dislocations ($\tau_{xz}^{inf}(d,w)$), where d is the spacing between individual pairs of dislocations and w is an appropriate average width of the fault ribbons [30]. With the shear modulus µ and the Burgers vector b we obtain Eqs. 1 and 2:

$$\tau_{xz}^{fin}(d,w) = \frac{\mu \cdot b}{2 \cdot \pi} \cdot \sum_{i=-N}^{N} \frac{1}{w + i \cdot d}. \quad (1)$$

$$\tau_{xz}^{inf}(d,w) = \frac{\mu \cdot b}{2 \cdot d} \cdot \frac{\sin(-2 \cdot \pi \cdot w/d)}{1 - \cos(-2 \cdot \pi \cdot w/d)}. \quad (2)$$

In Eq. 1, i is the summation index, which sums up the individual stress contributions provided by the blue dislocations of family 1.

Note that the scenario shown in Fig. 1d assumes a symmetrical distribution of red dislocations with respect to the central origin dislocation. Therefore, the contributions of all red dislocations cancel, and only the blue dislocations contribute to the stress field at the origin. This is reflected in both formulas Eqs. 1 and 2. There are only three APB-coupled dislocation pairs of family 1 embedded in the central ordered region while the dislocation network extends further up and down, Fig. 1a. In our calculation we can account for distant dislocation pairs. Fig. 4 shows that their contribution saturates when N > 5. The results in Fig. 4 were obtained using the projection corrected microstructural parameters w = 17.1 nm and d = 56.3 nm (obtained from experimental STEM images taken at **g**5) using a shear modulus µ of 79 GPa [32].

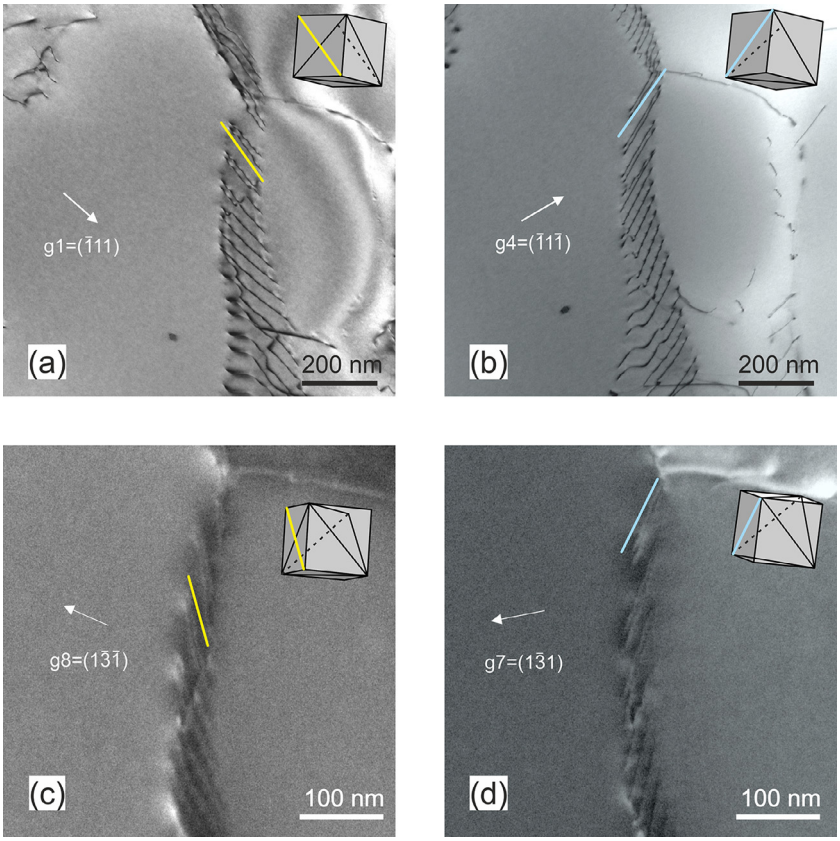

Fig. 3. STEM micrographs taken under four different contrast conditions. (a) $\mathbf{g}_1 = (\bar{1}\,1\,1)$, yellow lines: dislocation family 2 nearly parallel to $[\bar{1}01]$. (b) $\mathbf{g}_4 = (\bar{1}\,1\,\bar{1})$, blue lines: dislocation family 1 nearly parallel to [101]. Both families are in full contrast in (c) $\mathbf{g}_6 = (2\bar{2}0)$ and (d) $\mathbf{g}_{10} = (3\bar{1}1)$. (For interpretation of the references to color in this figure legend, the reader is referred to the web version of this article.).

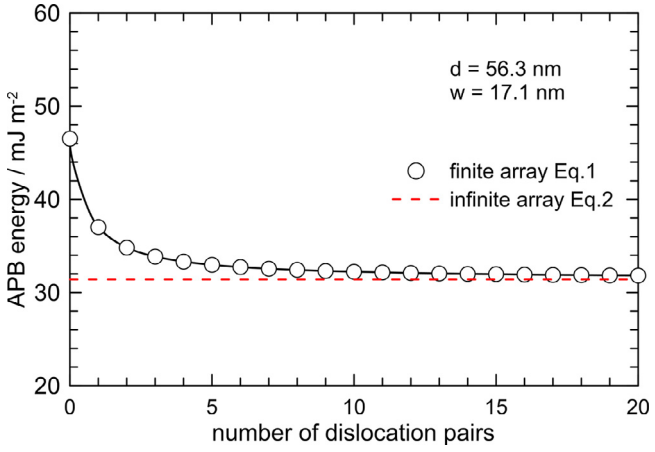

Fig. 4. Dependence of the APB energy on the number of dislocation pairs considered in the calculations, Eq. 1. The dashed red line represents the APB energy obtained for infinite dislocation array, Eq. 2.

As can be seen in Fig. 4, the finite solution converges for N>5, i.e. within a relative small microstructural distance. Based on the number of dislocation pairs considered in the calculations, our experimental results yield an APB-energy value in a range 30-46 mJm^{-2}, which is considerably lower than what has been reported in the literature in the context of creep properties, mostly considering a temperature range below 1000 °C [33–35]. These low values reflect the plane on which the APB fault lies which is (001) and is known to have a lower APB energy than the close-packed plane (111) which separates dislocations gliding on the slip plane. Studies of the relative energies based on binary Ni Al alloys predict that the ratio of fault energies $\frac{\gamma_{111}}{\gamma_{001}}$, is on the order of 1.5 to 2 [36]. This would correspond to a APB energy on the (111) plane of 45-92 mJm^{-2}, still lower that the values generally quoted at around 150 mJm^{-2}. Note that the current value is for a commercial superalloy whereas most measurements are for binary Ni-Al alloys of varying stoichiometry and some ternary alloys.

This lower than expected value may also result from the fact that under SLM processing conditions the dislocation network was equilibrated at temperatures above 1000 °C, where the ordering of the L_{12} phase has decreased [37–39] and will, in turn, lead to lower APB values. This implies that the observed dislocation pairs were unable to glide together as the sample cooled, because the dislocations are not on a glide plane, and the high temperature configuration has been frozen in. Note that the sample received a final 20 h anneal at 870 °C prior to examination. The movement of the dislocation pair from the low energy {001} plane to the {111} plane is the opposite of the cross-slip process accepted as the explanation of Kear–Wilsdorf locking [40]. A strong combination of the anisotropy of APB energy is combined with an equally strong torque force arising from the elastic anisotropy in nickel, known as the Yoo force [41], cause a glissile dislocation pair to cross-slip into a sessile configuration on the {001} plane.

Summary:

- A superalloy produced by SLM consists of many subgrains misoriented by less than a degree.
- These low angle grain boundaries pass through both the γ and the γ' phases.
- In the γ' phase the order leads to a pairing of alternate dislocations separated by APB faults.

- Measurement of the spacing in an array of two sets of screw dislocations representing a rotation of 0.5° about [001] has been related to the APB energy.
- The spacing, adjusted for the viewing directions yields an APB energy in a range 30–46 mJm^{-2} on the low energy (001) plane.
- This low value may reflect the inability of the pair to adjust during cooling.

Declaration of Competing Interest

The authors declare that they have no known competing financial interests or personal relationships that could have appeared to influence the work reported in this paper.

Acknowledgments

LH and GE acknowledge funding through project A2 of the collaborative research center SFB/TR 103 funded by the Deutsche Forschungsgemeinschaft DFG. AD acknowledges financial support through project ARMADIT no. CZ.02.1.01/0.0/0.0/16_025/0007304 and through infrastructural support by CEITEC. CMFR and CS acknowledge the support of Rolls-Royce plc and the EPSRC (Engineering and Physical Science Research Council) Strategic Partnership under EP/H022309/1 and EP/H500375/1. This work is published by permission of Siemens AG.

References

[1] R.C. Reed, The Superalloys – Fundamentals and Applications, Cambridge University Press, Cambridge, 2009.
[2] T.M. Pollock, S. Tin, J. Propulsion. Power 22 (2006) 361–374.
[3] H. Brooks, Metal Interfaces (Am. Society of Metals) (1952) 20.
[4] M. Probst-Hein A.Dlouhy, G. Eggeler, Acta Mater. 47 (1999) 2497.
[5] D.F. Lahrman, R.D. Field, R. Darolia, H.L. Fraser, Acta Metall. 36 (1988) 1309.
[6] L.E. Murr, S.M. Gaytan, D.A. Ramirez, E. Martinez, J. Hernandez, K.N. Amato, P.W. Shindo, F.R. Medina, R.B. Wicker, J. Mat. Sci. Tech. 28 (2012) 1–14.
[7] A. Hazotte, J. Lacaze, Scripta Met. 23 (1989) 1877–1882.
[8] P. Nörtershäuser, J. Frenzel, A. Ludwig, K. Neuking, G. Eggeler, Mat. Sci. Eng. A 626 (2015) 305–312.
[9] M. Feller Kniepmeier, T. Link, Mat. Sci. Eng. A 113 (1989) 191–195.
[10] R.D. Field, T.M. Pollock, W.H. Murphy, in: S.D. Antolovich Antolovich, R.W. Stusrud, R.A. MacKay, D.L. Anton, T. Khan, R.D. Kissinger, D.L. Klarstrom (Eds.), Superalloys, 1992, The Minerals, Metals and Materials Society, Warrendale, 1992, pp. 557–566.
[11] M. Kolbe, A. Dlouhy, G. Eggeler, Mat. Sci. Eng. A 246 (1998) 133–142.
[12] F.R.N. Nabarro, Met. Mat. Trans. A 27 (1996) 513–530.
[13] A. Epishin, T. Link, U. Bruckner, P.D. Portella, Acta Mater. 49 (2001) 4017–4023.
[14] K. Harris, G.L. Erickson, R.E. Schwer, in: M. Gell, C.S. Kortovich, R.H. Bricknell, W.B. Kent, J.F. Radavich (Eds.), Superalloys, 1984, The Minerals and Metals Society, Warrendale, 1984, pp. 221–230.
[15] R.K. Rai, J.K. Sahu, A. Pramanick, N. Paulose, D.C. Fernanod, S.K. Das, Mater. Charact. 150 (2019) 155–165.
[16] L. Van Belle, G. Vansteenkiste, J.C. Boyle, Key Eng. Mater. 554-557 (2013) 1828–1834.
[17] N. Siredey, M. Boufoussi, S. Denis, J. Lacaze J. Cryst. Growth 130 (1993) 132–146.
[18] Y.J. Lu, S.Q. Wu, Y.L. Gang, T.T. Huang, C.G. Yang, J.J. Li, J.X. Lin, Opt. Laser Technol. 75 (2015) 197–206.
[19] L.A. Jácome, P. Nörtershäuser, J.K. Heyer, A. Lahni, J. Frenzel, A. Dlouhy, C. Somsen, G. Eggeler, Acta Mater. 61 (2013) 2926–2943.
[20] X. Wu, P. Wollgramm, C. Somsen, A. Dlouhy, A. Kostka, G. Eggeler, Acta Mater. 112 (2016) 242–260.
[21] A. Dlouhy, G. Eggeler, Pract. Metallogr. 34 (1996) 629–642.
[22] L.A. Jácome, G. Eggeler, A. Dlouhy, Ultramicroscopy 122 (2012) 48–59.
[23] W. Bollmann, Crystalline Defects and Crystalline Interfaces, Springer Verlag, New York, 1970.
[24] T. Schober, R.W. Balluffi, Phil. Mag. 21 (1969) 109–123.
[25] E. Martinez, J.P. Hirth, M. Nastasi, A. Cari, Phys. Rev. B 85 (2012) 060101.
[26] D. Schwartz, V. Vitek, A.P. Sutton, Phil. Mat. A 51 (1985) 499–520.
[27] J. Th. M. De Hosson, V. Vitek, Phil. Mag. 61 (1990) 305–327.
[28] T.M. Pollock, R.D. Field, in: F.R.N. Nabarro, M.S. Duesbery (Eds.), Dislocations in Solids, Elsevier Sciences, 2002, pp. 547–618.
[29] G. Herrmann, H. Gleiter, G. Bäro, Acta Metall. 24 (1976) 353–359.
[30] P. Anderson, J.P. Hirth, J. Lothe, Theory of Dislocations, Cambridge University Press, Cambridge, 2017.
[31] X. Luan, H. Qin, F. Liu, Z. Dai, Y. Yi, Q. Li, Crystals 8 307 (2018) 1–11.
[32] S.V. Prikhodko, J.D. Carnes, D.G. Isaak, H. Yang, A.J. Ardell, Met. Mat. Trans. A 30 (1999) 2403–2408.
[33] N. Baluc N, H.P. Karnthaler, M.J. Mills, Phil. Mag. 64 (1991) 137–150.
[34] J. Sun, C.S. Lee, J.K.L. Lai, J.S. Wu, Intermetallics 7 (1999) 1329–1335.
[35] M.S. Titus, Y.M. Eggeler, A. Suzuki, T.M. Pollock, Acta Mater. 82 (2015) 530–539.
[36] D.M. Dimiduk, A.W. Thompson, Phil Mag. A 67 (3) (1993) 675–698.
[37] A. Kozubski, Progr. Mat. Sci. 41 (1997) 1–59.
[38] A.V. Ruban, H.L. Skriver, Phys. Rev. B 55 (1997) 856–874.
[39] H. Lang, H. Uzawa, T. Mori, W. Pfeiler, Intermetallics 9 (2001) 9–24.
[40] B.H. Kear, Acta Metall. 12 (1964) 555–569.
[41] M.H. Yoo, Acta Metall. 35 (1987) 1559–1569.